Nanoscale

COMMUNICATION

Carving growing nanocrystals: coupling seed-mediated growth with oxidative etching†

Esteban Villarreal, Guangfang Grace Li and Hui Wang *

Cite this: *Nanoscale*, 2018, **10**, 18457

Received 26th August 2018,
Accepted 14th September 2018

DOI: 10.1039/c8nr06895j

rsc.li/nanoscale

This work presents multiple experimental evidences coherently showing that the versatile structural evolution of Au nanocrystals during seed-mediated growth under the guidance of foreign metal ions and halide-containing surfactants is essentially dictated by the dynamic interplay between oxidative etching and nanocrystal growth. Coupling nanocrystal growth with oxidative etching under kinetically controlled conditions enables the *in situ* surface carving of the growing nanocrystals, through which the surface topography of shape-controlled nanocrystals can be deliberately tailored on the nanometer length-scale.

Precise geometry control of nanocrystals through deliberately designed colloidal syntheses forms the keystone for the fine-tuning and rational optimization of the plasmonic and catalytic properties of metallic nanoparticles for widespread applications in nanophotonics,[1] molecular sensing,[2] catalysis,[3] and biomedicine.[4] Fundamentally intriguing and methodologically invaluable to the colloidal nanoscience communities has been the seed-mediated growth of metallic nanocrystals exhibiting thermodynamically unexpected anisotropic geometries.[5–23] The remarkable level of precision and the versatility of geometry control realized through seed-mediated growth has been best manifested by the controlled transformations of preformed isotropic Au nanocrystal seeds into an entire family of geometrically distinct anisotropic Au nanostructures, such as nanorods,[5–8] nanoprisms,[9,10] nanobipyramids,[11] and high-index faceting nanopolyhedra,[12–16] under kinetically controlled conditions synergistically guided by foreign metal ions, most commonly Ag^+, and halide-containing surfactants, typically cetyltrimethylammonium bromide (CTAB) and cetyltrimethylammonium chloride (CTAC).

Although the seed-mediated synthetic protocols developed for various anisotropic nanocrystal geometries appear fairly similar at first glance, variation of any of the synthetic parameters, even to a slight degree, may drastically modify the shapes of the resulting nanocrystals.[13,17,18,23] Such subtlety and versatility of the syntheses are intrinsically tied to the mechanistic complexity of the seed-mediated nanocrystal growth processes. The mechanisms underlying the anisotropic structural evolution of Au nanoparticles have so far been discussed mainly in the context of shape-controlled nanocrystal growth dictated not only by the crystallographic habit of the parental seeds but also more profoundly by the structure-directing additives that regioselectively and dynamically passivate the surfaces of the evolving nanocrystals.[5–23] Several critical aspects regarding the detailed shape-evolving mechanisms, such as the driving force for symmetry-breaking, the structural dynamics at the evolving particle/solution interfaces, and the exact roles of Ag^+ foreign cations and the halide counter ions of the surfactants, however, have long been intensively debated and still remain ambiguous.[6,17,18,24–28] According to the shape-defining rules proposed by Mirkin and coworkers,[17] the seed-mediated shape evolution of multifaceted Au nanocrystals is essentially dictated by the underpotential deposition (UPD) of Ag adatoms on Au nanocrystal surfaces, which selectively stabilizes certain types of crystallographic facets. The halide anions, on the other hand, regulate the Au deposition kinetics by forming complexes with ionic gold species and further modulate the coverage and stability of the Ag UPD adlayer through surface capping. Previous experimental observations and computational results suggest that a strong synergy exists between the Ag UPD layer and the surface-capping halide anions.[6,17,18,25] While the above-mentioned shape-defining rules seem broadly applicable when interpreting ample examples in the literature, our observations reported here strongly indicate that the growth of Au nanocrystals is entangled with oxidative etching under the Ag^+- and CTAC-coguided seed-mediated growth conditions, and thus is mechanistically even more complicated than researchers typically thought. To fully decipher the complex mechanisms underpinning the intriguing structural evolution of nanocrys-

Department of Chemistry and Biochemistry, University of South Carolina, Columbia, South Carolina 29208, USA. E-mail: wang344@mailbox.sc.edu

†Electronic supplementary information (ESI) available. See DOI: 10.1039/c8nr06895j

tals during seed-mediated growth, oxidative etching must be added as a pivotal missing piece to the puzzle.

We employed CTAC-capped Au colloids (~4 nm in diameter, see Fig. S1 in the ESI†) as the seeds to guide the shape evolution of Au nanocrystals at room temperature under ambient air in aqueous growth solutions containing $HAuCl_4$ as the ionic gold precursor, CTAC as a surface-capping surfactant, ascorbic acid (AA) as a mild reducing agent, $AgNO_3$ as the source of Ag^+ foreign ions, and HCl as a pH regulator. In the absence of seeds, $AuCl_4^-$ was first reduced by AA to form $AuCl_2^-$, which was further reduced to metallic Au upon the addition of seeds to the growth solution.[6,13,18] The rate of the seed-mediated Au reduction was pH dependent, increasing with the pH of the growth solution.[6,17,18,28] On the other hand, the O_2 dissolved in the growth solution was capable of mildly oxidizing the Au atoms on the surfaces of the growing nanocrystals to form $AuCl_2^-$ with the aid of Cl^- as the complexing agent through the following reaction:[29]

$$4Au + O_2 + 8Cl^- + 4H^+ \rightarrow 4AuCl_2^- + 2H_2O$$

This etching process could be kinetically boosted by simply decreasing the pH of the growth solution without introducing any additional strong oxidants. As demonstrated by Wang, Stucky, and coworkers,[29] preformed single-crystalline Au nanorods underwent a shortening process driven by selective etching along their longitudinal axis in the presence of dissolved O_2 and CTAC or CTAB in an acidic environment. Xia and coworkers[30–32] also employed halide anions and O_2 in polyol solvents as mild etchant pairs to carve the surfaces of metallic nanocrystals in a site-selective manner. Here, we used HCl as a unique synthetic knob to tune the relative rates of oxidative etching *vs.* nanocrystal growth, through which we were able to fine-tailor the surface topography of nanocrystals adopting several primary geometries, such as quasi-spheres, cubes, and cuboctahedra, by controllably carving the surfaces of the growing nanocrystals *in situ*.

Increase of the HCl concentration, C_{HCl}, in the growth solution sped up the oxidative etching while simultaneously slowing down the nanocrystal growth. We systematically varied the C_{HCl} in the range of 0–25 mM while fixing the concentrations of $HAuCl_4$, $AgNO_3$, CTAC, and AA at 500 μM, 50 μM, 100 mM, and 1.2 mM, respectively. After the reactions proceeded for 16 h, we kinetically trapped the resulting nanostructures by separating them from their native growth solutions through centrifugation followed by redispersion in water. As revealed by the scanning electron microscopy (SEM) images in Fig. 1A–G, alteration of C_{HCl} markedly modified the shapes and surface topography of the resulting nanocrystals. At C_{HCl} below 3 mM, the isotropic seeds evolved into surface-roughened quasi-spherical nanoparticles (SRQSNPs, Fig. 1A and B) as a consequence of mild etching of fast-growing nanocrystals. In the intermediate C_{HCl} regime (5–15 mM), the etching effects became more pronounced, resulting in surface-textured concave nanocubes (STCNCs, Fig. 1C–E), which were derived from nanocubes through selective corrosion of the {100} side facets coupled with preferential Au deposition on the edges. When C_{HCl} was further increased to above 15 mM, oxidative etching became even faster while nanocrystal growth was further slowed down, leading to the formation of excavated cuboctahedral nanoparticles (ECONPs, Fig. 1F and G), a geometry derived from a nano-cuboctahedron by creating indentation on the {100} facets while retaining the {111} facets at the truncated corners.

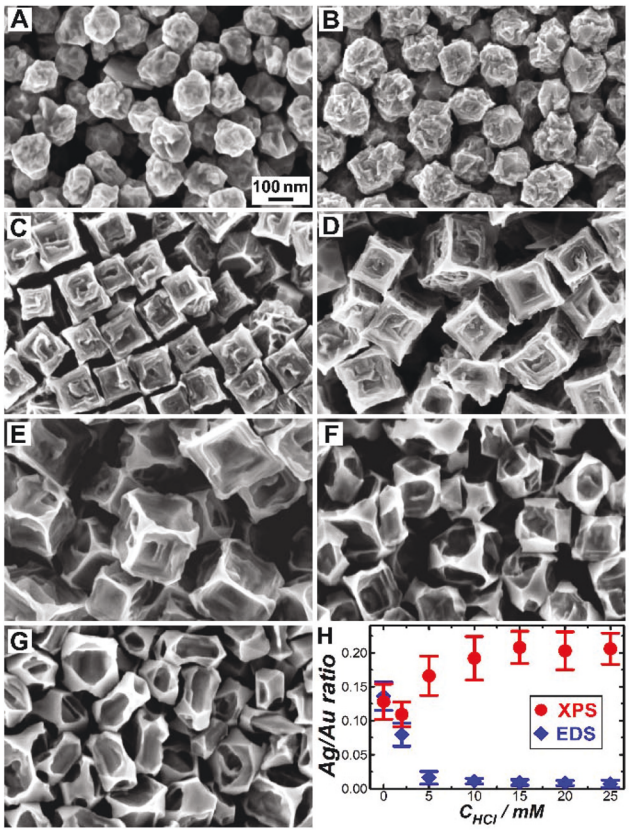

Fig. 1 SEM images of nanoparticles synthesized after 16 h in growth solutions containing 100 mM CTAC, 50 μM $AgNO_3$, 500 μM $HAuCl_4$, and 1.2 mM AA at various C_{HCl} values: (A) 0, (B) 2, (C) 5, (D) 10, (E) 15, (F) 20, and (G) 25 mM. All SEM images share the same scale bar in panel A. (H) Ag/Au atomic ratios quantified by XPS (red circles) and EDS (blue rhombi) for nanoparticles synthesized at various C_{HCl} values. The error bars represent the standard deviations obtained from 3 samples synthesized under identical conditions.

We used X-ray photoelectron spectroscopy (XPS) and energy dispersive spectroscopy (EDS) to characterize the surface and bulk compositions of the nanoparticles, respectively. In comparison with the XPS features of bulk Ag and Au foils, the Ag 3d peaks of the nanoparticle samples significantly downshifted by ~0.4 eV, while the Au 4f peaks slightly upshifted by less than ~0.05 eV (Fig. S2†), indicating the atomic intermix of Ag with Au either on the surfaces or in the sub-surface regions of the nanocrystals.[13,28] While Ag signals were clearly resolvable using XPS on all samples, Ag became almost undetectable using EDS on the samples synthesized at C_{HCl} above 5 mM (Fig. S3†). In Fig. 1H, we compared the surface and bulk Ag/Au

atomic ratios quantified using XPS and EDS, respectively, for the nanoparticle samples obtained at various C_{HCl} values. At C_{HCl} below 5 mM, EDS and XPS gave nominally the same Ag/Au atomic ratios (in the range of ~0.08–0.15), indicating that the SRQSNPs were essentially composed of Au–Ag alloys rather than phase-segregated core–shell heterostructures. Such an alloy structure was further confirmed by EDS elemental mapping (Fig. S4†). For the nanoparticles synthesized at C_{HCl} above 5 mM, the EDS signals of Ag became vanishingly weak while the surface Ag/Au atomic ratios quantified using XPS remained in the range of 0.15–0.22, strongly indicating that Ag existed as a UPD atomic adlayer on the nanocrystal surfaces. The structural transition from Au–Ag alloy nanocrystals to Ag adatom-capped Au nanocrystals as C_{HCl} increased could be well interpreted as a consequence of the pathway switch from Au–Ag codeposition to Ag UPD-mediated Au deposition. Detailed mechanisms underpinning this pathway switch were recently elucidated by our group using shape-controlled nanorod overgrowth as a prototypical system.[28]

To gain further insights into the temporal evolution of nanoparticle morphologies, we kinetically trapped the nanocrystals at various stages during the reactions. At the early stages of the reactions, the growth of nanocrystals was much faster than oxidative etching. As the reactions further proceeded, the nanocrystal growth became progressively slower due to the continuous consumption of $AuCl_2^-$, eventually approaching an equilibrium when the growth and etching rates became equivalent. At C_{HCl} of 2 mM, the seeds rapidly evolved into SRQSNPs and the nanoscale surface textures were well-preserved throughout the entire growth/etching process (Fig. 2A–D). The particle sizes rapidly increased before reaching a plateau after ~2 h (Fig. S5A†). When C_{HCl} was raised to 10 mM, the seeds first transformed into concave nanocubes enclosed by indented side facets, followed by nanoscale texturing of the nanocrystal surfaces (Fig. 2E–H). As the reactions proceeded, the degree of surface indentation increased, accompanied by progressive increase of the edge-lengths of STCNCs (Fig. S5B†). Concave nanocubes were also found to be the early-stage intermediates during the reactions at C_{HCl} of 20 mM. Under these conditions, fast etching of the slowly growing nanocrystals led to not only the indentation of the side facets but also the preferential oxidation of the undercoordinated surface atoms at the corners of the cube-shaped nanocrystals (Fig. 2I–L). Therefore, well-defined, thermodynamically favored {111} facets gradually developed at the truncated corners when the nanocrystal growth became sufficiently slow with respect to etching at the late stages of the reactions.

We tracked the temporal evolution of the nanocrystal compositions *ex situ* using XPS and EDS (Fig. S6†). The Ag/Au stoichiometric ratios of the alloy SRQSNPs remained essentially unchanged during seed-mediated growth, suggesting that Au and Ag were deposited at a constant relative rate. When the nanocrystal shape evolution was dominated by Ag-UPD, the Ag adatom coverage on the nanoparticle surfaces (quantified using XPS) increased over time until reaching equilibria, while the Ag signals remained almost undetectable by EDS throughout the entire processes. We also used inductively coupled plasma mass spectrometry (ICP-MS) to quantify the total amounts of gold and silver remaining in the supernatant at various reaction times after separating the nanocrystals from the growth solutions (Fig. S7†). At C_{HCl} of 2 mM, the total amounts of both gold and silver in the growth solutions progressively decreased until reaching the deposition/etching equilibrium as a consequence of seed-mediated Au–Ag co-deposition. When Ag UPD-mediated Au deposition occurred at C_{HCl} values of 10 and 20 mM, the gold precursors were gradually consumed while the total amount of silver species in the growth solutions remained almost unchanged. The structural evolution of the nanocrystals was further monitored *in situ* using optical extinction spectroscopy without separating the nanocrystals from their growth solutions. As shown in Fig. S8,† the increase of particle sizes, development of surface concavity, and introduction of surface textures all led to the spectral redshift and the broadening of the plasmon resonance peaks, whereas the plasmon resonances blue-shifted upon corner truncation. The temporal evolution of the extinction spectroscopic features is discussed in greater detail in the ESI.†

Increasing the AA concentration, C_{AA}, while keeping the other synthetic parameters unchanged allowed us to accelerate the nanocrystal growth without modifying the etching rate. At

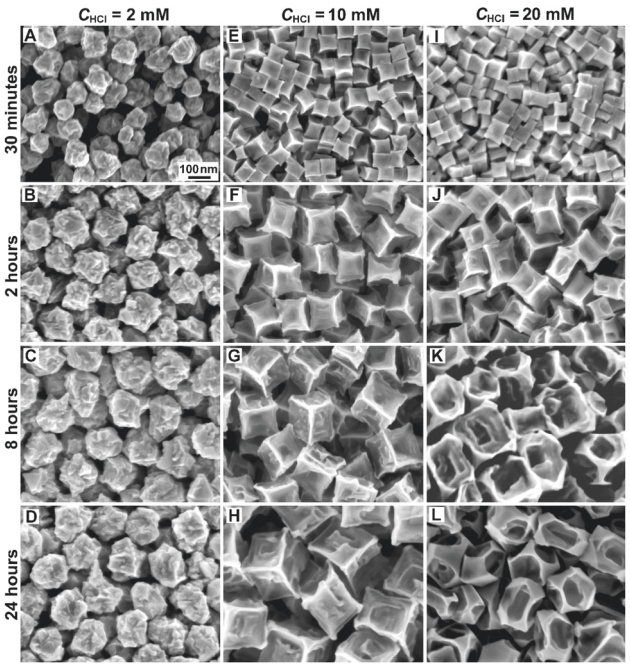

Fig. 2 SEM images of nanoparticles synthesized in growth solutions containing 50 μM $AgNO_3$, 500 μM $HAuCl_4$, 100 mM CTAC, and 1.2 mM AA at different C_{HCl} values after various reaction times: (A) 2 mM HCl, 0.5 h; (B) 2 mM HCl, 2 h; (C) 2 mM HCl, 8 h; (D) 2 mM HCl, 24 h; (E) 10 mM HCl, 0.5 h; (F) 10 mM HCl, 2 h; (G) 10 mM HCl, 8 h; (H) 10 mM HCl, 24 h; (I) 20 mM HCl, 0.5 h; (J) 20 mM HCl, 2 h; (K) 20 mM HCl, 8 h; and (L) 20 mM HCl, 24 h. All SEM images share the same scale bar in panel A.

C_{HCl} of 2 mM, the surface roughness of the nanocrystals could be tailored by varying the relative growth and etching rates, achieving the highest degree of surface texturing within a C_{AA} window of 1–2 mM (Fig. S9A–S9C†). At C_{HCl} of 20 mM, structural transitions from ECONPs to STCNCs and eventually to SRQSNPs were observed as C_{AA} progressively increased from 1 to 5 mM (Fig. S9D–S9F†) due to acceleration of nanocrystal growth. The oxidative etching could also be kinetically modulated without changing the nanocrystal growth rate by simply varying the concentration of O_2 dissolved in the growth solution. Saturating the growth solution with O_2 resulted in loss of nanoscale surface textures and decrease of particle sizes (Fig. S10A–S10C†) due to enhanced oxidative etching. When the growth solution was purged with N_2 to eliminate the dissolved O_2, the oxidative etching was effectively suppressed and the surface-roughened quasi-spherical morphology was preserved over a broad C_{HCl} range even up to 20 mM (Fig. S10D–S10F†). Interestingly, both the surface and bulk Ag/Au atomic ratios of the nanocrystals appeared almost independent of the concentration of O_2 dissolved in the growth solution (Fig. S11†), indicating that the nanocrystal compositions were essentially determined by the relative Ag and Au deposition rates rather than the relative rates of etching *vs.* growth.

While the effects of Ag^+ foreign ions on the seed-mediated growth of Au nanocrystals of various shapes have been well-documented in the literature,[6,17,18,24–28] we found that the Ag^+ foreign ions also played crucial roles in guiding the regioselective etching of nanocrystal surfaces. At C_{HCl} of 20 mM, the degree of corner truncation increased while the surface concavity decreased as the $AgNO_3$ concentration, C_{Ag}, progressively increased in the range of 20–60 μM (Fig. 3A–C). The increase of C_{Ag} resulted in a higher coverage of Ag UPD adatoms on the side facets of a cube-shaped nanoparticle, effectively slowing down the surface indentation process. However, the undercoordinated surface atoms located around the corners of a cube-shaped nanocrystal still remained prone to etching. Preferential etching of the corners with respect to the side facets, coupled with preferential Au deposition on the edges, led to the formation of ECONPs. When C_{HCl} decreased to 10 mM, the surfaces of the STCNCs became less concave and increasingly smoother while the sharp corners were still preserved as the surface coverage of Ag adatoms increased (Fig. 3D–F), primarily due to slower etching of the corners and side facets. Removal of $AgNO_3$ from the growth solution resulted in faster oxidative etching, drastically modifying the structure-transforming process. Under the Ag-free conditions, the Au seeds evolved into SRQSNPs at low C_{HCl}. As C_{HCl} increased, the feature sizes of surface textures increased and well-defined crystallographic facets started to develop on the nanocrystal surfaces, resulting in blue-shift of the plasmon resonance in the extinction spectra (Fig. S12†).

We further compared the post-synthetic etching of preformed Au concave nanocubes and Au–Ag alloy SRQSNPs in etching solutions containing 100 mM CTAC and 10 mM HCl, either with or without 50 μM $AgNO_3$. Apparently, the etching proceeded significantly faster in the Ag-free environment,

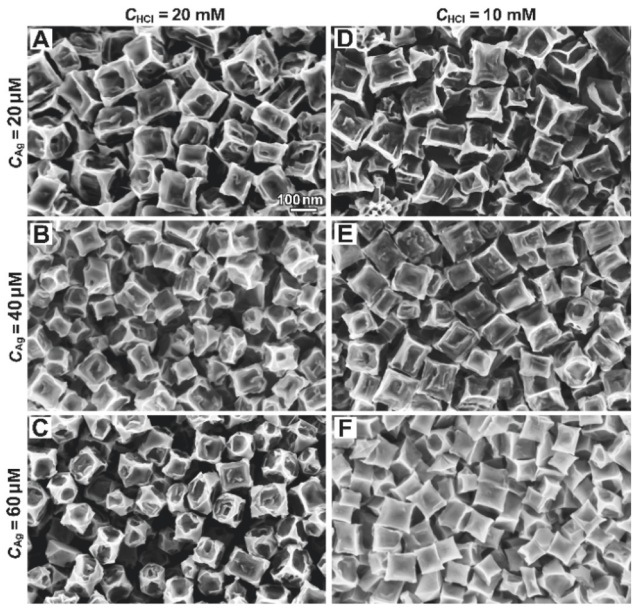

Fig. 3 SEM images of nanoparticles synthesized after 16 h in growth solutions containing 100 mM CTAC, 500 μM $HAuCl_4$, 1.2 mM AA, and various concentrations of HCl and $AgNO_3$: (A) 20 mM HCl, 20 μM $AgNO_3$; (B) 20 mM HCl, 40 μM $AgNO_3$; (C) 20 mM HCl, 60 μM $AgNO_3$; (D) 10 mM HCl, 20 μM $AgNO_3$; (E) 10 mM HCl, 40 μM $AgNO_3$; and (F) 10 mM HCl, 60 μM $AgNO_3$. All SEM images share the same scale bar in panel A.

resulting in more drastic decrease of the particle sizes (Fig. S13†). The Au SRQSNPs synthesized in the absence of Ag^+ foreign ions appeared even more vulnerable to oxidative etching than the Au–Ag alloy SRQSNPs, completely losing their surface textures after exposure to an etching solution containing 100 mM CTAC and 10 mM HCl under ambient air for 16 h (Fig. S14†). Therefore, the nanoscale surface textures were essentially a unique structural feature resulting from *in situ* mild surface etching of nanocrystals growing at appropriate rates.

In summary, multiple observations coherently indicate that oxidative etching interplays with nanocrystal growth under kinetically controlled conditions to guide the versatile structural evolution of Au nanocrystals during seed-mediated growth. This work provides important implications that may help us more comprehensively understand the seed-mediated growth of complex nanostructures when revisiting previously reported examples in the literature. Seed-mediated growth of various anisotropic nanostructures, such as nanorods and nanoprisms, may all involve site-selective etching of the growing nanocrystals, especially at the early stages when the symmetry of the isotropic seeds gets broken.[6,9,10,26,27] Another interesting example is the overgrowth of concave nanocube seeds into hollow Au nano-octahedra in a growth solution containing AA and HCl at a significantly higher $AgNO_3/HAuCl_4$ ratio of 1 : 1.[33] While the formation of the hollow octahedral nanoparticles was previously interpreted as the consequence of Ag UPD-stabilized {111} facet growth at the corners of the

concave nanocube seeds, it is highly likely that oxidative etching is also responsible for the growth of the intraparticle cavities. Here we have demonstrated that the nanoscale surface topography of shape-controlled nanocrystals can be fine-tailored through deliberate kinetic control of oxidative etching with respect to nanocrystal growth. Introduction of nanoscale surface textures to sub-wavelength metallic nanoparticles greatly expands the plasmonic tuning range and enhances the local electric fields exploitable for plasmon-enhanced spectroscopies.[34] In addition, surface-textured metallic nanoparticles may serve as an ideal model system for us to study how nanoscale surface texturing affects the light scattering properties of roughened nanostructures naturally existing in environmental and biological systems,[35] such as atmospheric dust particles and subcellular organelles. Furthermore, the surface-textured nanocrystals are enclosed by highly abundant undercoordinated surface atoms, which may serve as the active sites for heterogeneous catalysis.[36] Combination of desired plasmonic and catalytic properties on the same metallic nanocrystals further enables us to monitor intriguing catalytic molecular transformations in real time using plasmon-enhanced Raman scattering as a time-resolving and molecular finger-printing spectroscopic tool.[37–39] As exemplified by this work and several previous publications,[30,40–42] judiciously coupling nanocrystal growth with oxidative etching, galvanic replacement, or other redox processes enables the controlled synthesis of structurally sophisticated nanocrystals exhibiting exotic geometries and fine-tailored surface topography, greatly enhancing our capabilities to further fine-optimize the optical and catalytic properties of nanoparticles for specific applications.

Conflicts of interest

There are no conflicts to declare.

Acknowledgements

This work was supported by the National Science Foundation through an EPSCoR RII Track-I Award (OIA-1655740). E. V. was partially supported by a GAANN Fellowship provided by the Department of Education through the GAANN Award P200A120075.

Notes and references

1 A. Moreau, C. Ciraci, J. J. Mock, R. T. Hill, Q. Wang, B. J. Wiley, A. Chilkoti and D. R. Smith, *Nature*, 2012, **492**, 86–89.
2 J. N. Anker, W. P. Hall, O. Lyandres, N. C. Shah, J. Zhao and R. P. Van Duyne, *Nat. Mater.*, 2008, **7**, 442–453.
3 C. Chen, Y. J. Kang, Z. Y. Huo, Z. W. Zhu, W. Y. Huang, H. L. L. Xin, J. D. Snyder, D. G. Li, J. A. Herron, M. Mavrikakis, M. F. Chi, K. L. More, Y. D. Li, N. M. Markovic, G. A. Somorjai, P. D. Yang and V. R. Stamenkovic, *Science*, 2014, **343**, 1339–1343.
4 P. K. Jain, X. H. Huang, I. H. El-Sayed and M. A. El-Sayed, *Acc. Chem. Res.*, 2008, **41**, 1578–1586.
5 B. Nikoobakht and M. A. El-Sayed, *Chem. Mater.*, 2003, **15**, 1957–1962.
6 S. E. Lohse and C. J. Murphy, *Chem. Mater.*, 2013, **25**, 1250–1261.
7 J. Perez-Juste, I. Pastoriza-Santos, L. M. Liz-Marzan and P. Mulvaney, *Coord. Chem. Rev.*, 2005, **249**, 1870–1901.
8 L. Scarabelli, A. Sanchez-Iglesias, J. Perez-Juste and L. M. Liz-Marzan, *J. Phys. Chem. Lett.*, 2015, **6**, 4270–4279.
9 J. E. Millstone, S. J. Hurst, G. S. Metraux, J. I. Cutler and C. A. Mirkin, *Small*, 2009, **5**, 646–664.
10 L. Scarabelli, M. Coronado-Puchau, J. J. Giner-Casares, J. Langer and L. M. Liz-Marzan, *ACS Nano*, 2014, **8**, 5833–5842.
11 M. Z. Liu and P. Guyot-Sionnest, *J. Phys. Chem. B*, 2005, **109**, 22192–22200.
12 J. A. Zhang, M. R. Langille, M. L. Personick, K. Zhang, S. Y. Li and C. A. Mirkin, *J. Am. Chem. Soc.*, 2010, **132**, 14012–14014.
13 M. L. Personick, M. R. Langille, J. Zhang and C. A. Mirkin, *Nano Lett.*, 2011, **11**, 3394–3398.
14 Q. Zhang, N. Large and H. Wang, *ACS Appl. Mater. Interfaces*, 2014, **6**, 17255–17267.
15 T. Ming, W. Feng, Q. Tang, F. Wang, L. D. Sun, J. F. Wang and C. H. Yan, *J. Am. Chem. Soc.*, 2009, **131**, 16350–16351.
16 T. T. Tran and X. M. Lu, *J. Phys. Chem. C*, 2011, **115**, 3638–3645.
17 M. R. Langille, M. L. Personick, J. Zhang and C. A. Mirkin, *J. Am. Chem. Soc.*, 2012, **134**, 14542–14554.
18 S. E. Lohse, N. D. Burrows, L. Scarabelli, L. M. Liz-Marzan and C. J. Murphy, *Chem. Mater.*, 2014, **26**, 34–43.
19 Y. N. Xia, X. H. Xia and H. C. Peng, *J. Am. Chem. Soc.*, 2015, **137**, 7947–7966.
20 C. J. DeSantis, A. A. Peverly, D. G. Peters and S. E. Skrabalak, *Nano Lett.*, 2011, **11**, 2164–2168.
21 R. G. Weiner, M. R. Kunz and S. E. Skrabalak, *Acc. Chem. Res.*, 2015, **48**, 2688–2695.
22 W. X. Niu, W. Q. Zhang, S. Firdoz and X. M. Lu, *J. Am. Chem. Soc.*, 2014, **136**, 3010–3012.
23 T. K. Sau and C. J. Murphy, *J. Am. Chem. Soc.*, 2004, **126**, 8648–8649.
24 J. A. Edgar, A. M. McDonagh and M. B. Cortie, *ACS Nano*, 2012, **6**, 1116–1125.
25 N. Almora-Barrios, G. Novell-Leruth, P. Whiting, L. M. Liz-Marzan and N. Lopez, *Nano Lett.*, 2014, **14**, 871–875.
26 M. J. Walsh, S. J. Barrow, W. M. Tong, A. M. Funston and J. Etheridge, *ACS Nano*, 2015, **9**, 715–724.
27 M. J. Walsh, W. M. Tong, H. Katz-Boon, P. Mulvaney, J. Etheridge and A. M. Funston, *Acc. Chem. Res.*, 2017, **50**, 2925–2935.
28 Q. Zhang, H. Jing, G. G. Li, Y. Lin, D. A. Blom and H. Wang, *Chem. Mater.*, 2016, **28**, 2728–2741.

29 C. K. Tsung, X. S. Kou, Q. H. Shi, J. P. Zhang, M. H. Yeung, J. F. Wang and G. D. Stucky, *J. Am. Chem. Soc.*, 2006, **128**, 5352–5353.
30 Y. Q. Zheng, J. Zeng, A. Ruditskiy, M. C. Liu and Y. N. Xia, *Chem. Mater.*, 2014, **26**, 22–33.
31 M. C. Liu, Y. Q. Zheng, L. Zhang, L. J. Guo and Y. N. Xia, *J. Am. Chem. Soc.*, 2013, **135**, 11752–11755.
32 A. Ruditsicy, M. Vara, H. Huang and Y. N. Xia, *Chem. Mater.*, 2017, **29**, 5394–5400.
33 M. R. Langille, M. L. Personick, J. Zhang and C. A. Mirkin, *J. Am. Chem. Soc.*, 2011, **133**, 10414–10417.
34 Q. F. Zhang, N. Large, P. Nordlander and H. Wang, *J. Phys. Chem. Lett.*, 2014, **5**, 370–374.
35 H. Wang, K. Fu, R. A. Drezek and N. J. Halas, *Appl. Phys. B: Lasers Opt.*, 2006, **84**, 191–195.
36 Q. F. Zhang, D. A. Blom and H. Wang, *Chem. Mater.*, 2014, **26**, 5131–5142.
37 Q. F. Zhang, L. L. Han, H. Jing, D. A. Blom, Y. Lin, H. L. L. Xing and H. Wang, *ACS Nano*, 2016, **10**, 2960–2974.
38 Q. F. Zhang, Y. D. Zhou, E. Villarreal, Y. Lin, S. L. Zou and H. Wang, *Nano Lett.*, 2015, **15**, 4161–4169.
39 J. W. Zhang, S. A. Winget, Y. R. Wu, D. Su, X. J. Sun, Z. X. Xie and D. Qin, *ACS Nano*, 2016, **10**, 2607–2616.
40 Z. N. Wang, H. Wang, Z. R. Zhang, G. Yang, T. O. He, Y. D. Yin and M. S. Jin, *ACS Nano*, 2017, **11**, 163–170.
41 L. Polavarapu, D. Zanaga, T. Altantzis, S. Rodal-Cedeira, I. Pastoriza-Santos, J. Perez-Juste, S. Bals and L. M. Liz-Marzan, *J. Am. Chem. Soc.*, 2016, **138**, 11453–11456.
42 L. Chen, F. Ji, Y. Xu, L. He, Y. F. Mi, F. Bao, B. Q. Sun, X. H. Zhang and Q. Zhang, *Nano Lett.*, 2014, **14**, 7201–7206.

Electronic Supplementary Information for

Carving Growing Nanocrystals: Coupling Seed-Mediated Growth with Oxidative Etching

*Esteban Villarreal, Guangfang Grace Li, and Hui Wang**

Department of Chemistry and Biochemistry, University of South Carolina, Columbia, South Carolina 29208, United States

** To whom correspondence should be addressed.*

Email: wang344@mailbox.sc.edu; Phone: 1-803-777-2203; Fax: 1-803-777-9521.

S1. Experimental Details

S1.1. Chemicals and Materials

All reagents were used as received without further purification. Gold(III) chloride trihydrate ($HAuCl_4 \cdot 3H_2O$, ACS grade) was purchased from J.T. Baker. Sodium borohydride ($NaBH_4$, 99%), hydrochloric acid (HCl, 37%), and L-ascorbic acid (AA, 99.5%) were obtained from Sigma-Aldrich. Cetyltrimethylammonium chloride (CTAC, 96%) and silver nitrate ($AgNO_3$, 99.9995% metal basis) were obtained from Alfa Aesar. Ultrapure water (18.2 MΩ resistivity, Barnstead EasyPure II 7138) was used for all experiments.

S1.2. Synthesis of Au Seeds

Colloidal Au seeds (~ 4 nm in diameter) were synthesized by reducing $HAuCl_4$ with $NaBH_4$ in the presence of CTAC following a previously reported protocol.[1-3] Briefly, 0.25 mL of $HAuCl_4$ (10 mM) was introduced into an aqueous solution of CTAC (10 mL, 100 mM) under magnetic stir. Then 0.30 mL of ice cold, freshly prepared $NaBH_4$ (10 mM) was quickly added to the solution containing both CTAC and $HAuCl_4$. The mixture solution was stirred for 1 min, then left undisturbed for 2 h at room temperature under ambient air, and finally diluted 1000-fold with 100 mM CTAC. The diluted seed colloids were used for the subsequent seed-mediated growth of various nanostructures.

S1.3. Seed-Mediated Nanocrystal Growth

The shape-controlled nanocrystal growth was initiated by introducing 40 μL of the diluted Au seeds into an aqueous growth solution containing $HAuCl_4$, AA, HCl, $AgNO_3$, and CTAC. The total volume of the growth solution was 10 mL and the concentrations of CTAC and $HAuCl_4$ were kept at 100 mM and 500 μM, respectively. The concentrations of HCl, AA, and $AgNO_3$ were systematically varied to tune the rate of the nanocrystal growth relative to that of oxidative etching, based on which the shapes and surface topography of the resulting nanocrystals were fine-tailored. Upon the addition of seeds, the reactants were gently mixed for 30 s and then left undisturbed at room temperature under ambient air for various reaction times. To control the concentration of oxygen dissolved in the growth solutions, the solutions containing the reactants were purged with N_2 or O_2 for 1 h before mixing and the reaction mixtures were then kept under N_2 or O_2 atmospheres throughout the reaction processes. The as-obtained nanoparticles were washed with water 3 times through centrifugation/redispersion cycles, and finally redispersed in water.

S1.4. Structural Characterizations

The structures of the nanoparticles were characterized by scanning electron microscopy (SEM) using a Zeiss Ultraplus thermal field emission scanning electron microscope. The samples for SEM measurements were dispersed in water and drop-dried on silicon wafers. An energy dispersive spectroscopy (EDS) elemental analysis unit attached to the microscope was used to map the spatial distribution of Au and Ag elements in each nanoparticle. The bulk Ag:Au atomic ratios of various samples were quantified based on the relative areas of the Ag Lα and Au Lα peaks in the spectra. The Au seeds were imaged by transmission electron microscopy (TEM) using a Hitachi HT7800 transmission electron microscope, which was operated at an accelerating voltage of 120 kV. XPS measurements were carried out using a Krato AXIS Ultra DLD XPS system equipped with a monochromatic Al Kα source. The samples for XPS measurements were all freshly prepared and dried in vacuum before being loaded into the XPS chambers. The surface Ag:Au atomic ratios of various samples were quantified based on the relative areas of the Ag 3d and Au 4f peaks in the spectra. The sample penetration depth of the XPS measurements under the current experimental conditions was calibrated to be ~ 1 nm,[4] roughly corresponding to 5 atomic layers from the outer surface of the nanoparticles. Therefore, the formation of a saturated monolayer coverage of Ag UPD adatoms on the Au nanoparticles would ideally result in an Ag/Au

atomic ratio of ~ 0.25. The standard deviations of the Ag:Au atomic ratios quantified by EDS and XPS were obtained from 3 samples synthesized under identical conditions and shown as the error bars in Figure 1H, Figure S6, and Figure S11. The optical extinction spectra of the nanoparticles were measured on aqueous colloidal suspensions at room temperature using a Beckman Coulter Du 640 spectrophotometer. The total amounts of gold and silver remaining in the supernatant at various reaction times were quantified using a Finnigan ELEMENT XR double focusing magnetic sector field inductively coupled plasma-mass spectrometer (SF-ICP-MS) after separating the nanocrystals from the growth solutions.

S2. Additional Discussion of the Temporal Evolution of Optical Extinction Spectra

The surface-roughened quasi-spherical nanoparticles (SRQSNPs), surface-textured concave nanocubes (STCNCs), and excavated cuboctahedral nanoparticles (ECONPs) all exhibited plasmonic characteristics sensitively dependent upon their sizes, shapes, and surface topography. Therefore, the structural evolution of the nanocrystals could be monitored *in situ* using optical extinction spectroscopy without separating the nanocrystals from their growth solutions. The plasmon resonance band of the Au-Ag alloy SRQSNPs progressively red-shifted and broadened as the particle size increased (Figure S8A), in line with previous observations on the surface-roughened Au nanoparticles.[5] When the SRQSNPs became larger than ~ 150 nm, a spectral feature corresponding to the quadrupole resonance emerged around 650 nm in addition to the dipole resonance due to phase retardation effects.[6-9] For the STCNCs, the surface indentation led to spectral redshift of the plasmon resonance, while the nanoscale surface texturing caused significant broadening of the peaks (Figure S8B). During the growth of ECONPs, the plasmon resonance peak first underwent a red-shifting and broadening process due to surface indentation and texturing, and then blue-shifted upon corner truncation at the later stages of the reactions (Figure S8C). Besides the plasmon resonance peaks in the visible and near-infrared, the spectral feature in the wavelength range below 400 nm arose from the interband electronic transitions of Au. Because the intensity of extinction due to interband transitions was qualitatively proportional to the Au mass in the nanocrystals, the rate of the mass increase of growing nanocrystals could be straightforwardly tracked by monitoring the temporal evolution of the optical extinction at 350 nm (Figure S8D), which showed that the nanocrystal growth rates decreased with increase of HCl concentration.

S3. Additional Figures

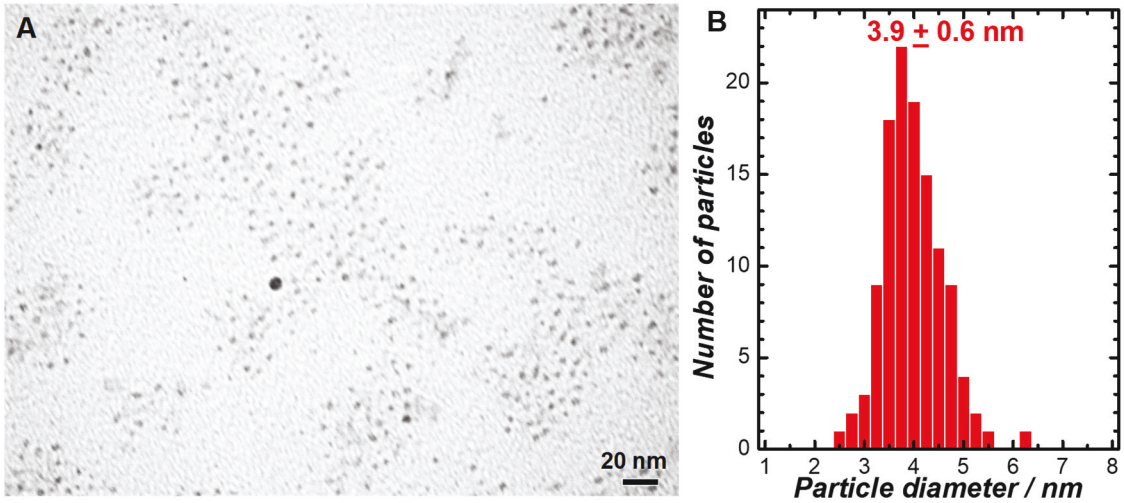

Figure S1. (A) TEM image and (B) size distribution of colloidal Au seeds.

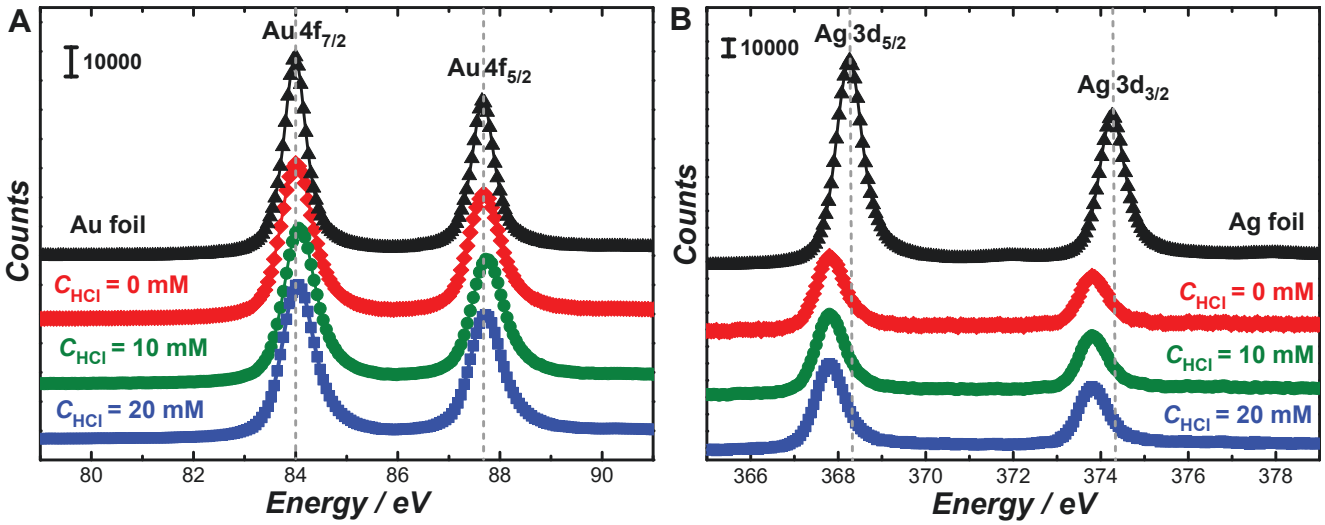

Figure S2. XPS spectra of (A) Au 4f and (B) Ag 3d regions of nanoparticles synthesized after 16 h in 100 mM CTAC, 50 μM $AgNO_3$, 500 μM $HAuCl_4$, and 1.2 mM AA in the presence of 0, 10, and 20 mM HCl. The spectra of a bulk Au foil and Ag foil were also shown for comparison. The spectra were offset for clarity.

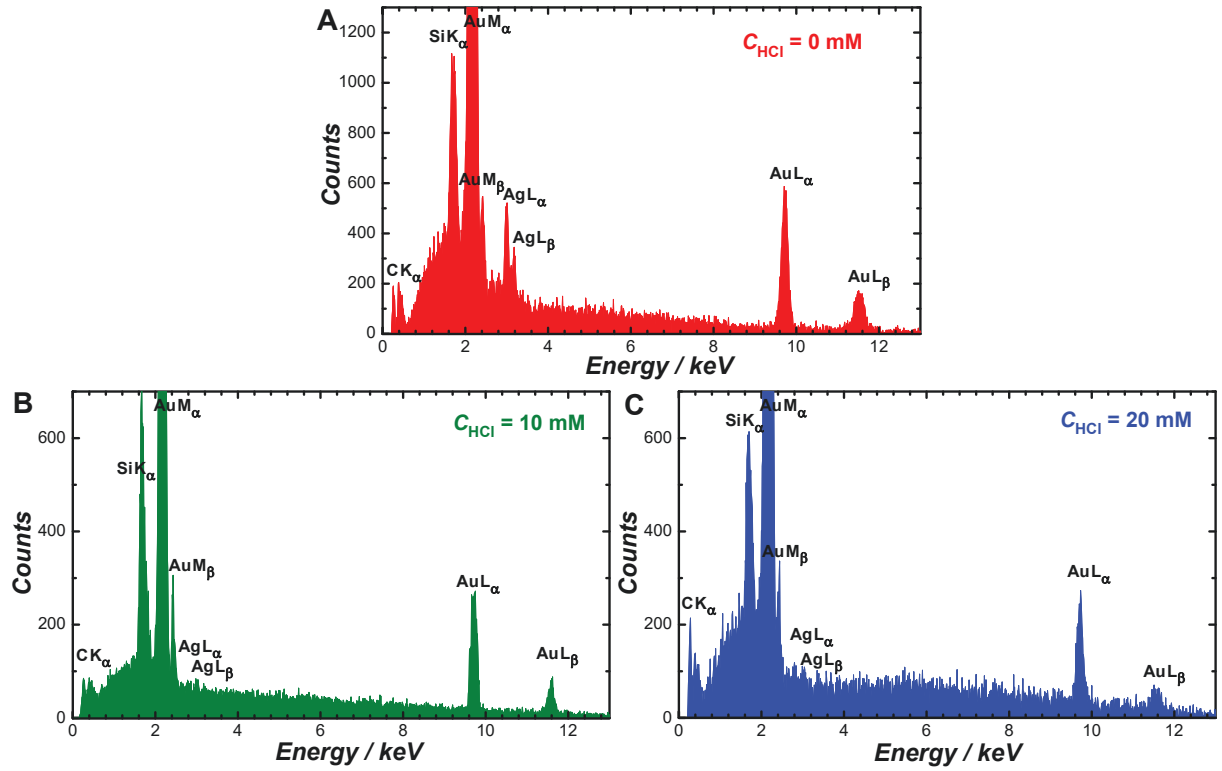

Figure S3. EDS spectra of nanoparticles synthesized after 16 h in 100 mM CTAC, 50 µM $AgNO_3$, 500 µM $HAuCl_4$, 1.2 mM AA, and (A) 0, (B) 10, and (C) 20 mM HCl. The Si signals were from the Si substrates.

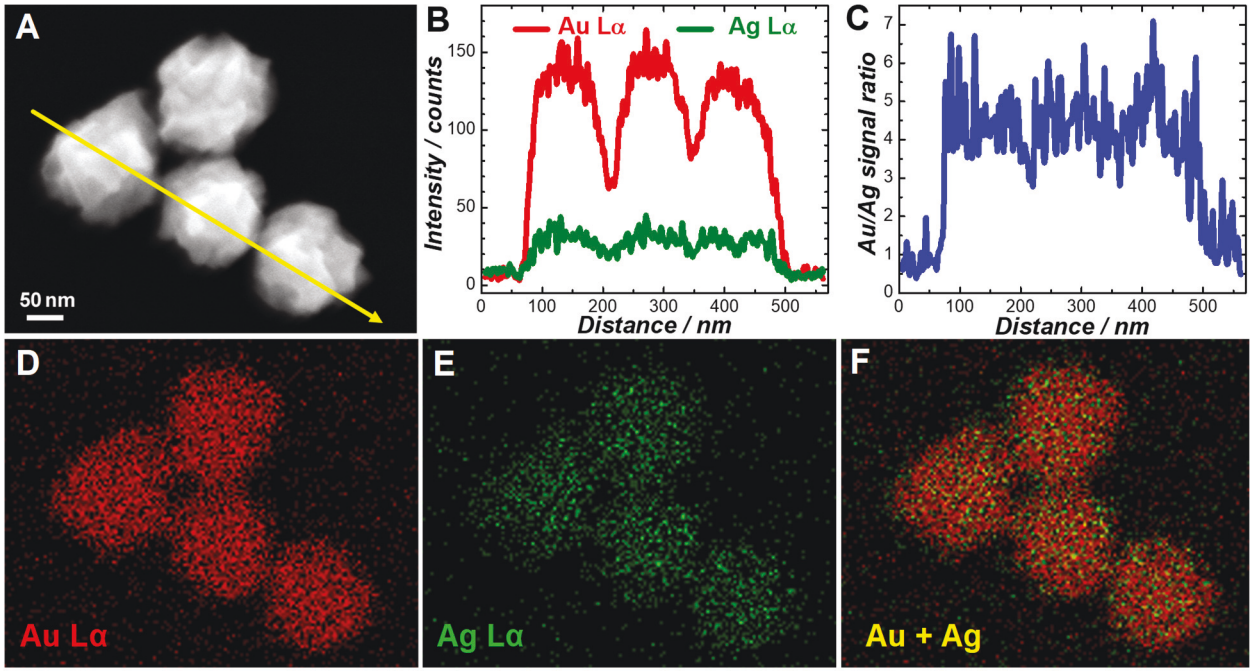

Figure S4. (A) SEM image of Au-Ag alloy surface-textured quasi-spherical nanoparticles synthesized after 16 h in a growth solution containing 100 mM CTAC, 50 µM $AgNO_3$, 500 µM $HAuCl_4$, and 1.2 mM AA. (B) Line-profiles of EDS intensities of Au Lα and Ag Lα, and (C) line-profile of Au/Ag signal ratios across the yellow line in panel A. EDS elemental maps of (D) Au, (E) Ag, and (F) overlay of Au + Ag.

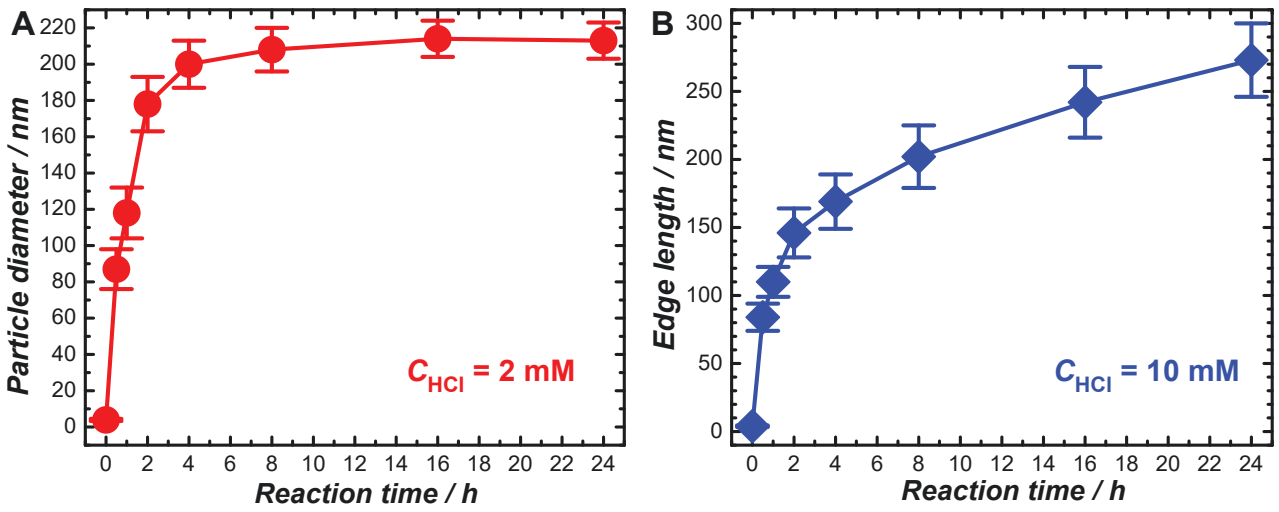

Figure S5. Temporal evolution of particle sizes during the seed-mediated nanocrystal growth in growth solutions containing 100 mM CTAC, 50 μM $AgNO_3$, 500 μM $HAuCl_4$, 1.2 mM AA, and (A) 2 and (B) 10 mM HCl. The average particle sizes and standard deviations were obtained from 100 particles in the SEM images for each sample. The Au seeds were 3.9 ± 0.6 nm in diameter.

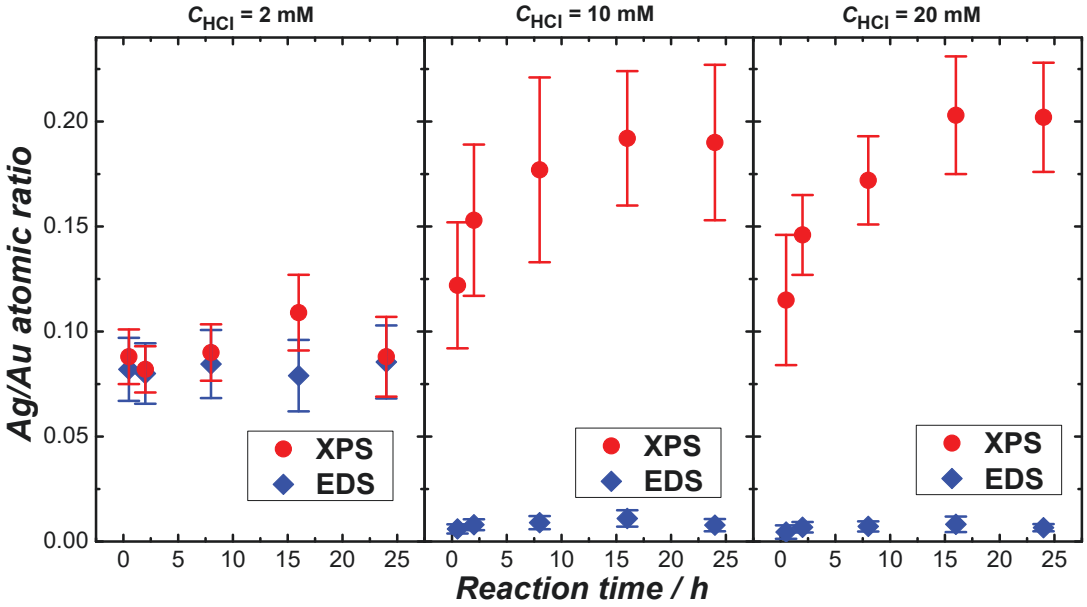

Figure S6. Temporal evolution of surface Ag/Au atomic ratio (quantified by XPS) and bulk Ag/Au atomic ratio (quantified by EDS) during seed-mediated nanocrystal growth in growth solutions containing 100 mM CTAC, 50 μM $AgNO_3$, 500 μM $HAuCl_4$, 1.2 mM AA, and (*left panel*) 2, (*middle panel*) 10, and (*right panel*) 20 mM HCl. The error bars represent the standard deviations obtained from 3 samples synthesized under identical conditions.

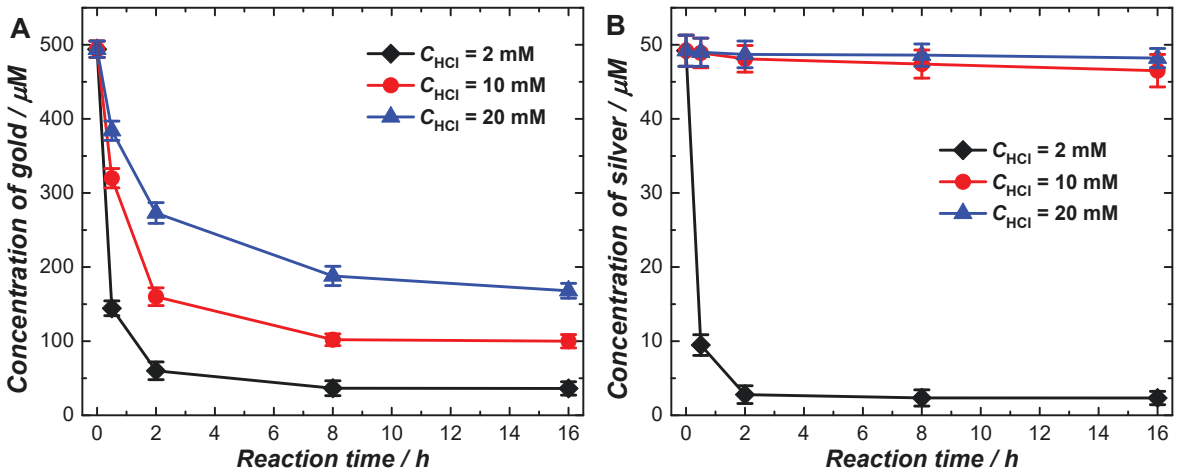

Figure S7. Total amounts of (A) gold and (B) silver remaining in the supernatant at various reaction times quantified by ICP-MS. The growth solutions contained 100 mM CTAC, 50 μM $AgNO_3$, 500 μM $HAuCl_4$, 1.2 mM AA, and 2, 10, or 20 mM HCl.

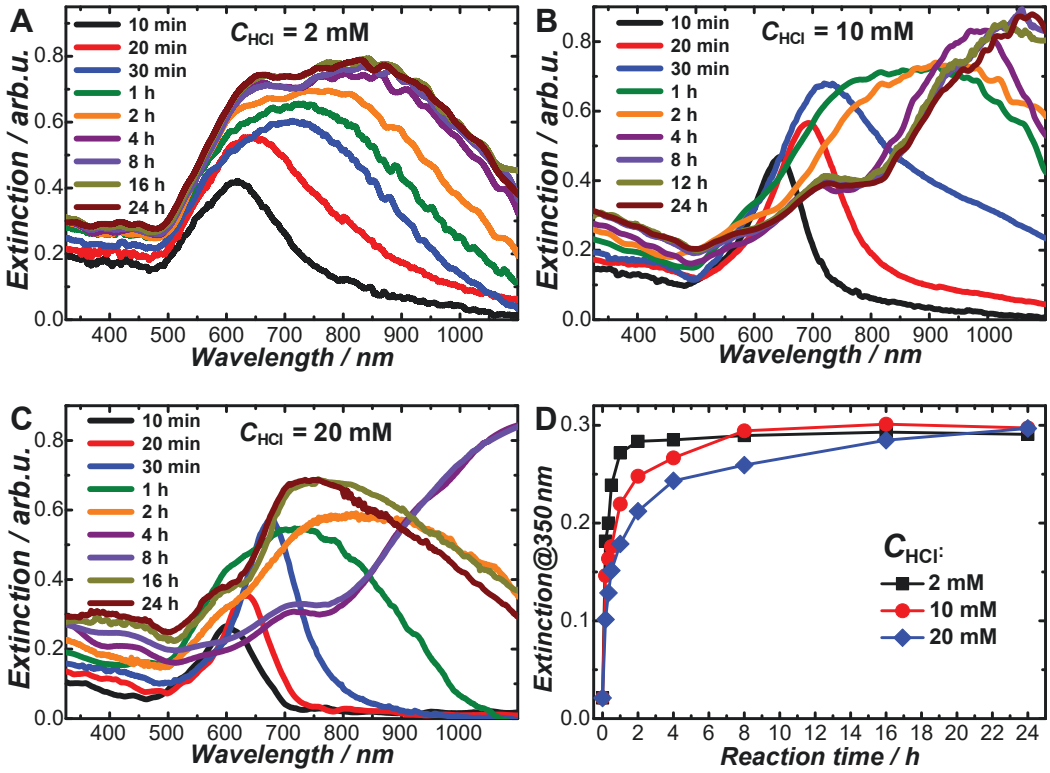

Figure S8. Temporal evolution of optical extinction spectra during nanocrystal growth in 100 mM CTAC, 50 μM $AgNO_3$, 500 μM $HAuCl_4$, 1.2 mM AA, and (A) 2 mM, (B) 10 mM, and (C) 20 mM HCl. (D) Temporal evolution of optical extinction at 350 nm.

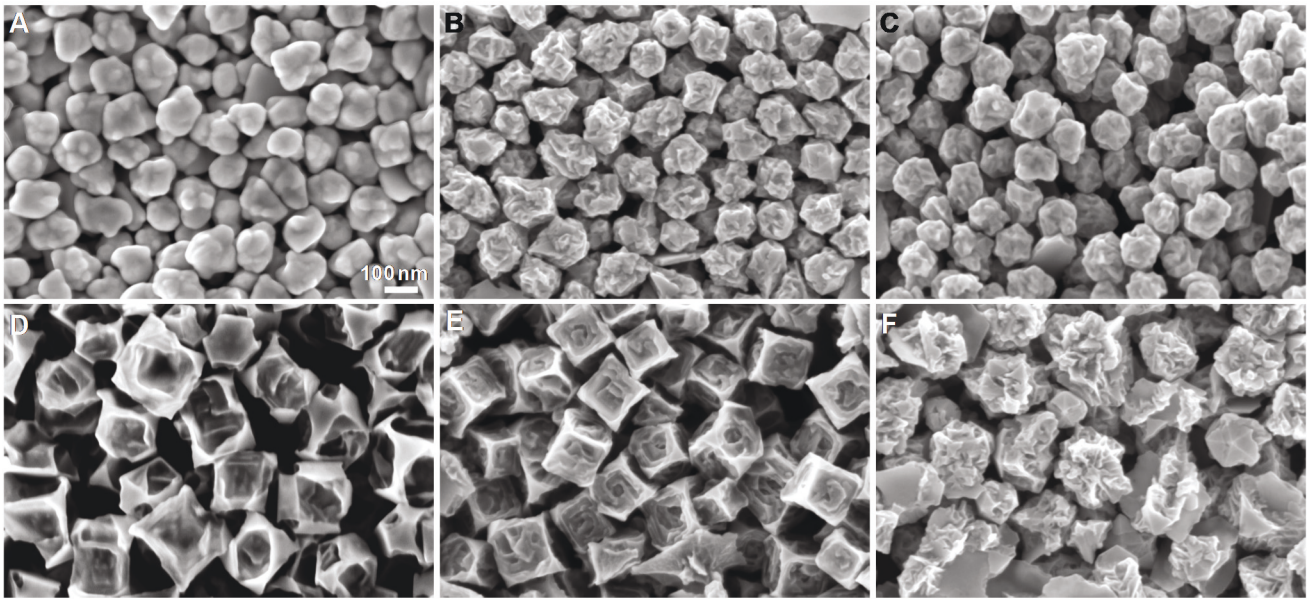

Figure S9. Effects of AA. SEM images of nanoparticles synthesized after 16 h in growth solutions containing 100 mM CTAC, 50 µM $AgNO_3$, 500 µM $HAuCl_4$, and various concentrations of AA and HCl: (A) 0.5 mM AA, 2 mM HCl; (B) 1 mM AA, 2 mM HCl; (C) 5 mM AA, 2 mM HCl; (D) 1 mM AA, 20 mL HCl; (E) 2.5 mM AA, 20 mL; (F) 5 mM AA, 20 mM HCl. All SEM images share the same scale bar in panel A.

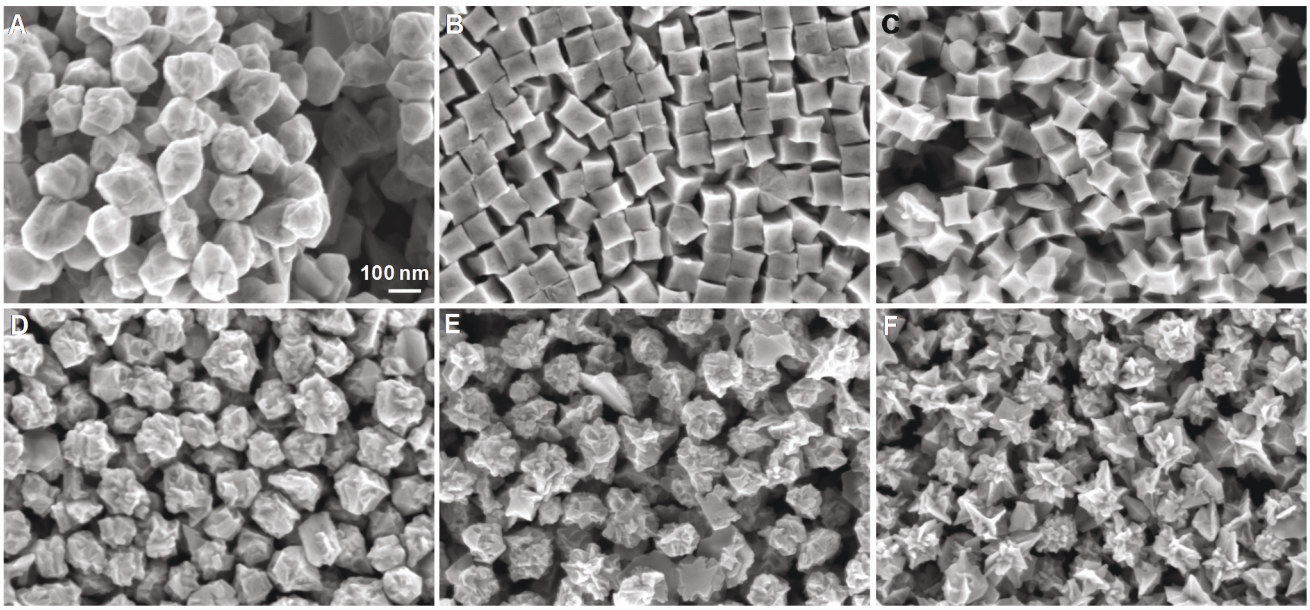

Figure S10. Effects of dissolved oxygen. SEM images of nanoparticles synthesized after 16 h in oxygen-purged growth solutions containing 100 mM CTAC, 50 µM $AgNO_3$, 500 µM $HAuCl_4$, 1.2 mM AA, and (A) 2, (B) 10, and (C) 20 mM HCl. SEM images of nanoparticles synthesis after 16 h in deoxygenated (purged with N_2) growth solutions containing 100 mM CTAC, 50 µM $AgNO_3$, 500 µM $HAuCl_4$, 1.2 mM AA, and (D) 2, (E) 10, and (F) 20 mM HCl. All SEM images share the same scale bar in panel A.

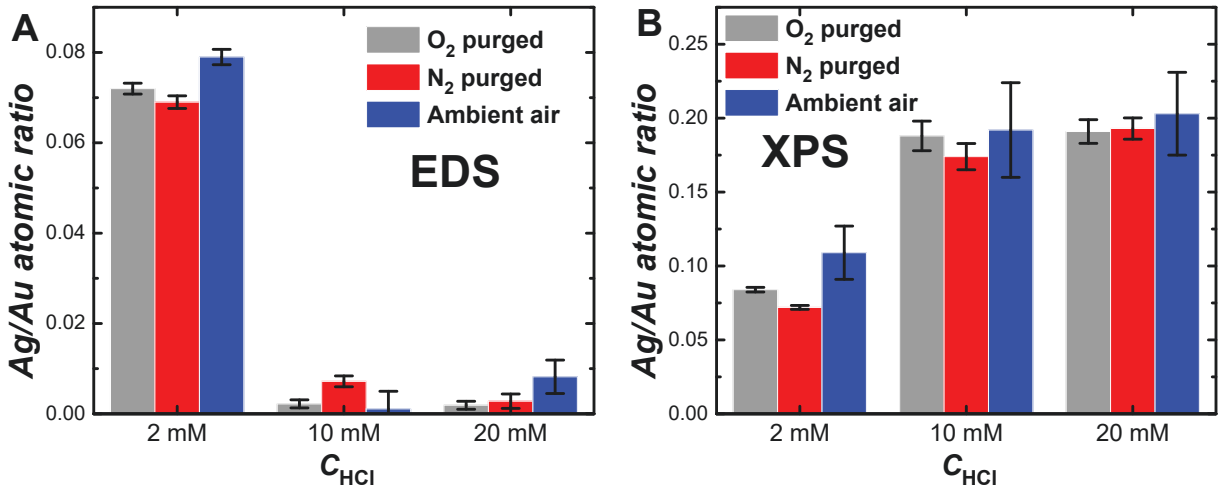

Figure S11. (A) Bulk Ag/Au atomic ratio quantified by EDS and (B) surface Ag/Au atomic ratio quantified by XPS for nanoparticle samples synthesized after 16 h in growth solutions containing 100 mM CTAC, 50 μM $AgNO_3$, 500 μM $HAuCl_4$, 1.2 mM AA, and 2, 10, and 20 mM HCl. The growth solutions were either exposed to ambient air or purged with O_2 or N_2. The error bars represent the standard deviations obtained from 3 samples synthesized under identical conditions.

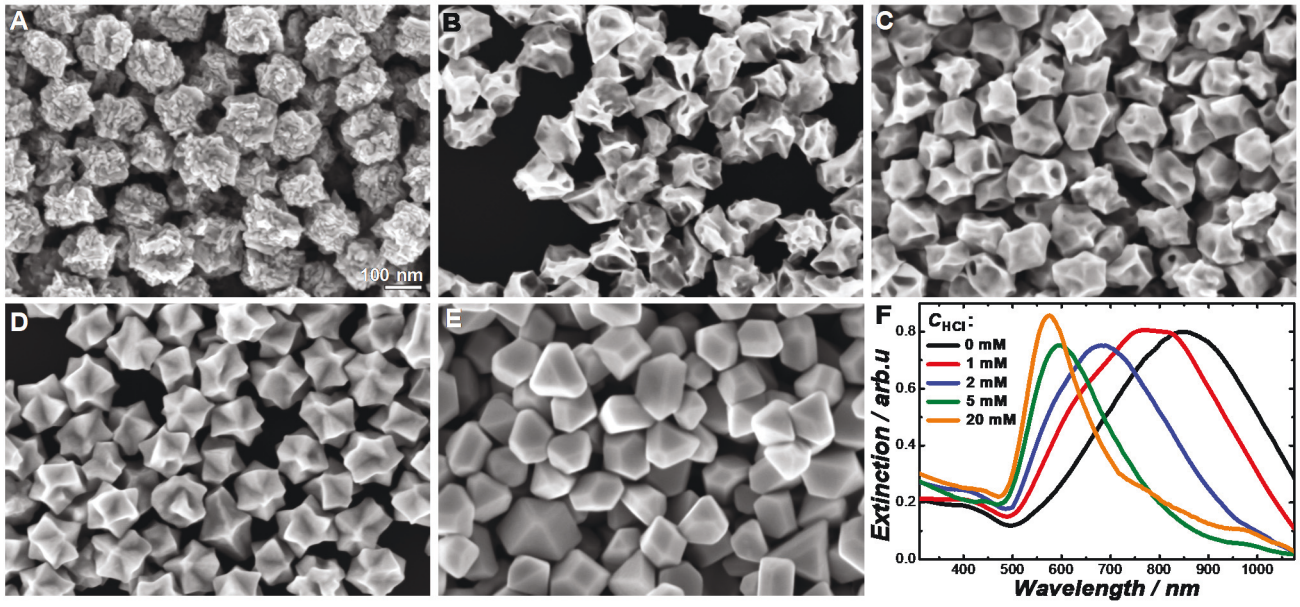

Figure S12. Etching and growth of Au nanoparticles in the absence of $AgNO_3$. Au nanoparticles synthesized after 16 h in growth solutions containing 100 mM CTAC, 500 μM $HAuCl_4$, 1.2 mM AA, and (A) 0, (B) 1, (C) 2, (D) 5, and (E) 20 mM HCl. All SEM images share the same scale bar in panel A. (F) Optical extinction spectra of colloidal Au nanoparticles synthesized after 16 h in growth solutions containing 100 mM CTAC, 500 μM $HAuCl_4$, 1.2 mM AA, and various concentrations of HCl as labeled in the figure.

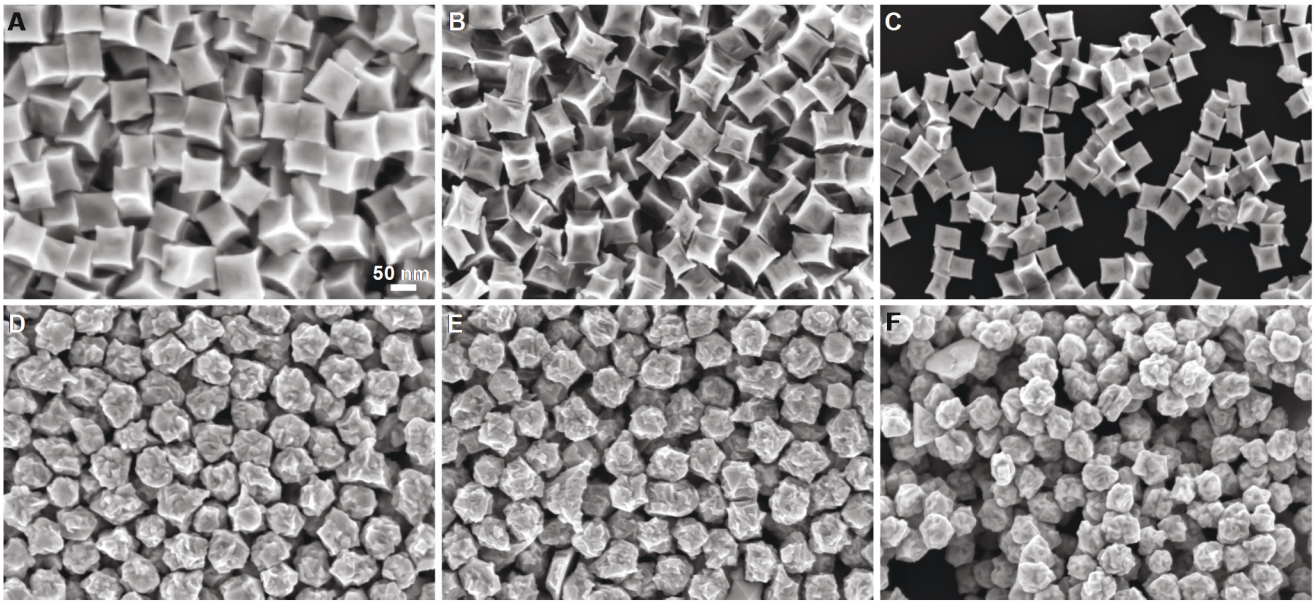

Figure S13. (A) SEM image of nanoparticles synthesized after 1 h in a growth solution containing 100 mM CTAC, 500 μM $HAuCl_4$, 50 μM $AgNO_3$, 1.2 mM AA, and 10 mM HCl. SEM images of the nanoparticles shown in panel A after post-synthetic etching for 16 h in etching solutions containing 100 mM CTAC and 10 mM HCl (B) in the presence of 50 μM $AgNO_3$ and (C) in the absence of $AgNO_3$. (D) SEM image of nanoparticles synthesized after 1 h in a growth solution containing 100 mM CTAC, 500 μM $HAuCl_4$, 50 μM $AgNO_3$, 1.2 mM AA, and 2 mM HCl. SEM images of the nanoparticles shown in panel D after post-synthetic etching for 16 h in etching solutions containing 100 mM CTAC and 10 mM HCl (E) in the presence of 50 μM $AgNO_3$ and (F) in the absence of $AgNO_3$. All SEM images share the same scale bar in panel A. In all these experiments, the preformed nanoparticles were first separated from their growth solution through centrifugation, then washed with water through redispersion and centrifugation, and finally redispersed in the etching solutions.

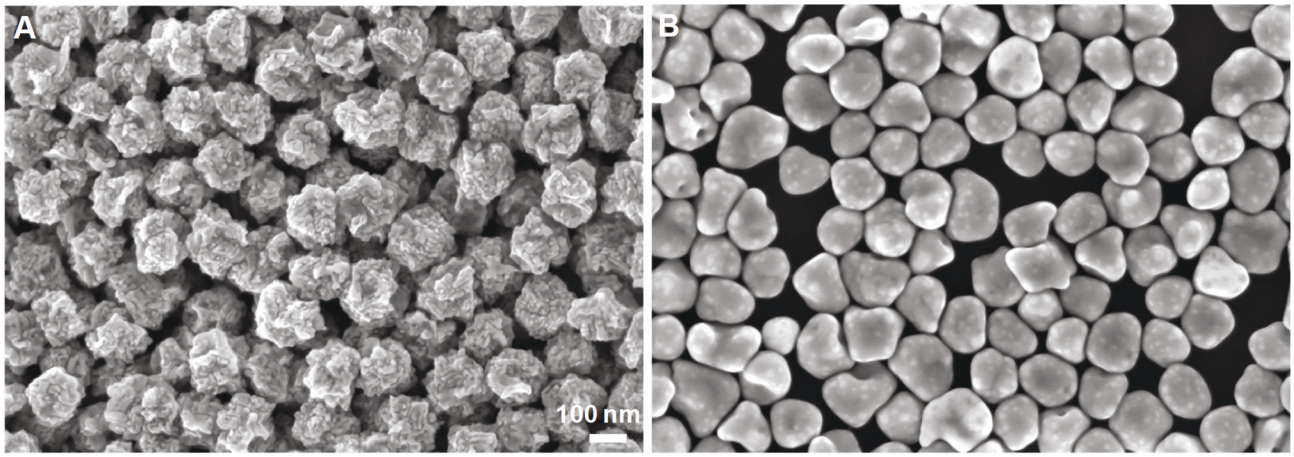

Figure S14. (A) SEM image of Au nanoparticles synthesized after 16 h in a growth solution containing 100 mM CTAC, 500 μM $HAuCl_4$, and 1.2 mM AA. (B) SEM image of the nanoparticles obtained after exposing the nanoparticles shown in panel A to an etching solution containing 100 mM CTAC and 10 mM HCl for 16 h. Both SEM images share the same scale bar in panel A.

S4. References for Electronic Supplementary Information

1. M. L. Personick, M. R. Langille, J. Zhang and C. A. Mirkin, *Nano Lett.*, 2011, **11**, 3394-3398.
2. J. Zhang, M. R. Langille, M. L. Personick, K. Zhang, S. Li and C. A. Mirkin, *J. Am. Chem. Soc.*, 2010, **132**, 14012-14014.
3. Q. F. Zhang, N. Large and H. Wang, *ACS Appl. Mater. Interfaces*, 2014, **6**, 17255-17267.
4. Q. F. Zhang, H. Jing, G. G. Li, Y. Lin, D. A. Blom and H. Wang, *Chem. Mater.*, 2016, **28**, 2728-2741.
5. Q. F. Zhang, N. Large, P. Nordlander and H. Wang, *J. Phys. Chem. Lett.*, 2014, **5**, 370-374.
6. J. E. Millstone, S. Park, K. L. Shuford, L. D. Qin, G. C. Schatz and C. A. Mirkin, *J. Am. Chem. Soc.*, 2005, **127**, 5312-5313.
7. H. Wei, A. Reyes-Coronado, P. Nordlander, J. Aizpurua and H. X. Xu, *ACS Nano*, 2010, **4**, 2649-2654.
8. H. Wang and N. J. Halas, *Adv. Mater.*, 2008, **20**, 820-825.
9. A. S. Kumbhar, M. K. Kinnan and G. Chumanov, *J. Am. Chem. Soc.*, 2005, **127**, 12444-12445.